Simulation of particle diversity and mixing state over Greater Paris: a model–measurement inter-comparison†

Shupeng Zhu,[a] Karine N. Sartelet,[*a] Robert M. Healy[b] and John C. Wenger[c]

Air quality models are used to simulate and forecast pollutant concentrations, from continental scales to regional and urban scales. These models usually assume that particles are internally mixed, *i.e.* particles of the same size have the same chemical composition, which may vary in space and time. Although this assumption may be realistic for continental-scale simulations, where particles originating from different sources have undergone sufficient mixing to achieve a common chemical composition for a given model grid cell and time, it may not be valid for urban-scale simulations, where particles from different sources interact on shorter time scales. To investigate the role of the mixing state assumption on the formation of particles, a size-composition resolved aerosol model (SCRAM) was developed and coupled to the Polyphemus air quality platform. Two simulations, one with the internal mixing hypothesis and another with the external mixing hypothesis, have been carried out for the period 15 January to 11 February 2010, when the MEGAPOLI winter field measurement campaign took place in Paris. The simulated bulk concentrations of chemical species and the concentrations of individual particle classes are compared with the observations of Healy *et al.* (*Atmos. Chem. Phys.*, 2013, **13**, 9479–9496) for the same period. The single particle diversity and the mixing-state index are computed based on the approach developed by Riemer *et al.* (*Atmos. Chem. Phys.*, 2013, **13**, 11423–11439), and they are compared to the measurement-based analyses of Healy *et al.* (*Atmos. Chem. Phys.*, 2014, **14**, 6289–6299). The average value of the single particle diversity, which represents the average number of species within each particle, is consistent between simulation and measurement (2.91 and 2.79 respectively). Furthermore, the average value of the mixing-state index is also well represented in the simulation (69% against 59% from the measurements). The spatial distribution of the mixing-state index shows that the

aCEREA (Joint Laboratory Ecole des Ponts ParisTech – EdF R& D), Université Paris-Est, Champs-sur-Marne, France. E-mail: sartelet@cerea.enpc.fr; Fax: +33 1 64 15 21 70; Tel: +33 1 64 15 21 57

bEnvironmental Monitoring and Reporting Branch, Ontario Ministry of the Environment and Climate Change, Toronto, Canada

cDepartment of Chemistry & Environmental Research Institute, University College Cork, Cork, Ireland

† Electronic supplementary information (ESI) available. See DOI: 10.1039/c5fd00175g

particles are not mixed in urban areas, while they are well mixed in rural areas. This indicates that the assumption of internal mixing traditionally used in transport chemistry models is well suited to rural areas, but this assumption is less realistic for urban areas close to emission sources.

1   Introduction

Atmospheric particles possess a large diversity of chemical compositions, which are constantly evolving as particles mix with each other and interact with surrounding gases. The diversity of particle compositions in a population of a given size range is often referred to as the particle mixing state.[1] Although most measurements are performed for "bulk" chemical compounds, *i.e.* without considering the particle mixing state (*e.g.*, Aerodyne high-resolution time-of-flight aerosol mass spectrometer (HR-ToF-AMS),[2] and multi-angle absorption photometer (MAAP)[3]), other field studies have focused on measuring individual particle compositions using single particle mass spectrometers such as the aerosol time-of-flight mass spectrometer (ATOFMS). Particle mixing state information can aid identification of particle sources,[4–7] as well as determine climate-relevant properties such as cloud condensation nuclei (CCN) activity, hygroscopicity, optical absorption and scattering.[8–11] Furthermore, information on the particle mixing state can be a powerful tool to assess ageing processes and the relative impact of local and regional sources of ambient particles in urban environments.[12]

Aside from *in situ* field observations, the modelling of composition-resolved particles remains challenging. In most air quality and climate models, for computational reasons, the particle diversity is not considered, and it is assumed that all particles within the same size bin[13] or within the same mode[14] have homogeneous composition. These models are often referred to as internal-mixing models. An external-mixing model provides additional complexity by allowing for multiple particle compositions within a given size range. Limited by complexity and computational resources, most of the developed external-mixing models are 0-D box models.[15–20] Few attempts have been made to simulate externally-mixed particles in three dimensions, usually neglecting coagulation, and introducing assumptions. In Kleeman and Cass,[21] different particle distributions were associated with different emission sources. However, particles were not allowed to exchange freely between different populations, and only transportation and interaction with gas phase species was simulated. In the works of Stier *et al.*[22] and Bauer *et al.*,[23] the particle distribution was represented by mixed and unmixed modes of predefined compositions; in Oshima *et al.*,[24] the compositions of particles were discretised based on the mass fraction of black carbon in the particles. Riemer *et al.*[25] modeled externally-mixed particles using an accurate stochastic approach, which might be computationally expensive when the number of particles is high. Zhu *et al.*[20] developed a Size-Composition Resolved Aerosol Model (SCRAM), where both the size and mass fractions of chemical components of particles are discretised. For a given particle size bin, particles have distinct chemical compositions. When discretising mass fractions, chemical components may be grouped into several aggregates to reduce the computational cost. SCRAM takes into account the processes of coagulation, condensation/evaporation and nucleation.

The SCRAM model has already been integrated into the Polyphemus air quality platform[26] and used to evaluate the particle properties in the Greater Paris region from 28 June to 5 July 2009.[27] This evaluation showed that SCRAM is able to give satisfactory results for both $PM_{2.5}/PM_{10}$ mass concentrations and aerosol optical depths, as assessed from comparisons with observations. Furthermore, the model has the ability to analyse the particle mixing state, as well as the impact of the mixing-state assumption on particle formation and properties. However, as no field measurements of single particle composition and mixing state are available for this period, the model performance could not be evaluated.[27] In this work, a simulation is conducted for January/February 2010 when the composition of individual particles was measured[1] during the winter campaign of MEGAPOLI (Megacities: emissions, urban, regional and Global Atmospheric POLlution and climate effects, and Integrated tools for assessment and mitigation). As a result, the model performance in simulating the particle mixing state can be evaluated for the first time through a model–measurement inter-comparison.

2   Model description

The Polair3D air quality model[28] of the Polyphemus air quality platform[26] is used to simulate air quality over the Paris area. The Carbon Bond 05 model (CB05)[29] is used for gas-phase chemistry and the VSRM model is applied for the in-cloud processing of aerosols.[30] The SCRAM model[27] is used to simulate the dynamics of the aerosol size distribution.

In SCRAM, the mass fraction of a given chemical component or aggregate of chemical components within each particle is discretised into bins. Compared to previous work,[20,27] SCRAM now allows the user to independently discretise the mass-fraction bins for each chemical component or aggregate of chemical components. In other words, the discretisation and the number of mass-fraction bins can be different for each chemical component or aggregate of chemical components. A comprehensive particle composition list is generated by selecting the possible combinations of the mass-fraction bins of each chemical component or aggregate of chemical components. A combination of mass fractions is defined as acceptable only if the sum of the lower bounds of each fraction bin within the combination is lower than 100%.

Three aerosol dynamic processes are taken into account in SCRAM: coagulation, condensation/evaporation and the homogeneous binary nucleation of sulfate and water. In this work, the condensation/evaporation of inorganic aerosols is determined using ISORROPIA[31] with a fully dynamic approach to compute dynamically the mass transfer rate between gas and particles for each particle size and composition bin. For secondary organic aerosol (SOA) formation, the H_2O model[32] is used, and bulk equilibrium is always assumed for organic species due to limitations of the H_2O model. After condensation/evaporation, the moving-center algorithm is used for mass-number redistribution among fixed size bins and composition bins. More details about the discretisation method, the mathematical derivation, the different condensation/evaporation approaches and model validations can be found in Zhu *et al.*[20]

Although SCRAM has the ability to simulate externally-mixed (EM) particles, it may also be used for internally-mixed (IM) particles, *i.e.* using the internal-mixing

assumption by having only one mass-fraction bin (between 0 and 100%) for each chemical component or aggregate of chemical components.

3   Simulation setup and measurement database

Simulations were conducted over Greater Paris between 15 January and 11 February 2010. The domain covers the whole Greater Paris region ([1.35°E, 3.55°E] × [48.00°N, 49.50°N]) with a horizontal resolution of 0.02° × 0.02°, and 9 vertical layers from ground level to 12 000 m.

In order to generate initial and boundary conditions for the simulation over Greater Paris, two nested simulations over Europe and France were conducted (see Fig. 1 for details of the domains). Because of the limitation of computational resources, these simulations were conducted with the internal-mixing assumption and the bulk-equilibrium approach for condensation/evaporation. The initial and boundary conditions for the Europe simulation were obtained from the Model for OZone And Related chemical Tracers (Mozart v2.0),[33] and those for the France simulation were obtained from the Europe simulation. For both the France and Europe simulations, anthropogenic emissions of gases and particles were taken from the EMEP inventory,[34] while the biogenic emissions were computed using the Model of Emissions of Gases and Aerosols from Nature (MEGAN).[35] Meteorology was from reanalysis of the European Centre for Medium-Range Weather Forecasts (ECMWF) model.

For the simulations over Greater Paris, the anthropogenic emissions of gases and particles were obtained from the Airparif (the Paris air quality agency, http://www.airparif.asso.fr) inventory for the year 2005 over Ile de France and from the EMEP inventory outside Ile de France. Following Couvidat et al.,[36] gas-phase semi-volatile organic compound (SVOC) emissions were estimated from primary
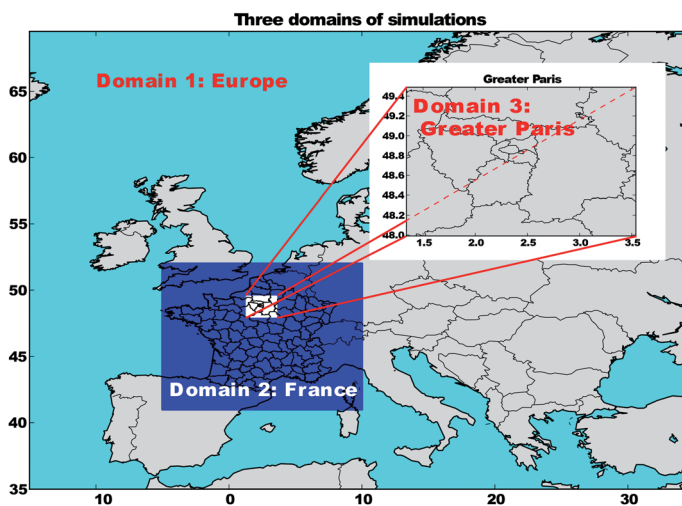

Fig. 1 Map of the three domains used for simulations: Europe ([−14.75°E, 34.75°E] × [35.25°N, 69.75°N], resolution: 0.5° × 0.5°), France ([−5.0°E, 10.0°E] × [41°N, 52°N], resolution: 0.1° × 0.1°) and Greater Paris ([1.35°E, 3.55°E] × [48.00°N, 49.50°N], resolution: 0.02° × 0.02°).

organic aerosol (POA) emissions. Although a ratio (SVOC Emissions/POA Emissions) of 5 was used in Couvidat et al.,[36] this ratio was set to 2.5 here, as derived from measurement data contained in a recent traffic emission report.[37] Meteorology was simulated with the Weather Research & Forecasting (WRF) version 3.6 model[38] using the urban canopy model and the Corine land-use database[39] with the YSU parametrization[40] for the planetary boundary layer. The WSM6 scheme[41] was used for the microphysics option of WRF, and the Kain–Fritsch convective parametrization[42] was used for cumulus physics.

Two simulations were conducted over Greater Paris: one with the internal-mixing (IM) assumption and one with the external-mixing (EM) assumption. The size distribution ranging from 0.01 to 10 μm was discretised into five size bins with bounds at 0.01, 0.1585, 0.4, 1.0, 2.5119 and 10 μm. As detailed in Couvidat et al.,[32] 31 particulate species were included in the simulations. In order to establish an appropriate comparison with the chemical species available from the observations, the 31 species were divided into 5 groups in the EM simulation: Elemental Carbon (EC), sulfate (SO_4), nitrate (NO_3), organic aerosol group (OA), and OThers (OT), which includes ammonium and sea salt. For the external-mixing (EM) simulation, the mass fraction of the first group, EC, was discretised into three mass-fraction bins ([0.0–0.1], [0.1–0.9], [0.9–1.0]), and the SO_4, NO_3 and OA groups were discretised into two mass-fraction bins ([0.0–0.1], [0.1–1.0]). If the mass fraction of one chemical group is located within the range [0.1–1.0], then it is considered as one of the main chemical groups of the bin, otherwise it is regarded as insignificant. EC was discretised with one more mass-fraction bin than the other groups ([0.9–1.0]), to be able to distinguish freshly emitted EC particles from aged particles. The last group OT was not discretised and its mass fraction was obtained by mass conservation. A total of 17 possible particle compositions were generated, as presented in Table 1. The names assigned to the

Table 1 17 Externally-mixed particle compositions

| Index | Composition names | Mass fraction of each group | | | |
		EC	SO_4	NO_3	OA
1	OT	0–0.1	0–0.1	0–0.1	0–0.1
2	OA	0–0.1	0–0.1	0–0.1	0.1–1
3	NO_3	0–0.1	0–0.1	0.1–1	0–0.1
4	OA–NO_3	0–0.1	0–0.1	0.1–1	0.1–1
5	SO_4	0–0.1	0.1–1	0–0.1	0–0.1
6	OA–SO_4	0–0.1	0.1–1	0–0.1	0.1–1
7	SO_4–NO_3	0–0.1	0.1–1	0.1–1	0–0.1
8	OA–SO_4–NO_3	0–0.1	0.1–1	0.1–1	0.1–1
9	EC+	0.1–0.9	0–0.1	0–0.1	0–0.1
10	EC–OA	0.1–0.9	0–0.1	0–0.1	0.1–1
11	EC–NO_3	0.1–0.9	0–0.1	0.1–1	0–0.1
12	EC–OA–NO_3	0.1–0.9	0–0.1	0.1–1	0.1–1
13	EC–SO_4	0.1–0.9	0.1–1	0–0.1	0–0.1
14	EC–OA–SO_4	0.1–0.9	0.1–1	0–0.1	0.1–1
15	EC–SO_4–NO_3	0.1–0.9	0.1–1	0.1–1	0–0.1
16	EC–OA–SO_4–NO_3	0.1–0.9	0.1–1	0.1–1	0.1–1
17	EC	0.9–1	0–0.1	0–0.1	0–0.1

particle compositions were chosen depending on their main chemical groups. The water content within each particle was also computed and tracked with SCRAM, while it was excluded when computing the mass fraction of each chemical group.

The measurement data of O_3, PM_{10} and $PM_{2.5}$ from the BDQA database ("Base de Données de la Qualité de l'Air": the French Database for Air Quality that covers France) are used to evaluate the model performance. More detailed observation data is obtained during the winter MEGAPOLI (Megacities: Emissions, urban, regional and Global Atmospheric POLlution and climate effects, and Integrated tools for assessment and mitigation) campaign in 2010,[12] where chemical composition at the single particle level was measured using an Aerosol Time-of-Flight Mass Spectrometer (ATOFMS) for particles within the size range 150–1067 (nm) at the urban background site of the Laboratoire d'Hygiène de la Ville de Paris (LHVP), Paris (48.75°N, 2.36°E) between 15 January and 11 February. Ten carbonaceous classes were identified from approximately 1.50 million detected mass spectra using a K-means algorithm.[43] First, the number concentration of each ATOFMS class was calculated for each hour of the campaign, then the corresponding mass concentration of each particle class was estimated based on particle diameter and an assumed density value of 1.5 g cm^{-3}. The hourly-resolved mass fraction of each chemical species was also measured for each size bin, which helped determine the bulk mass concentration of each species during the measured period. Finally, the ATOFMS-derived total mass concentrations for each species were multiplied by a factor of 1.24 to account for the low bias of the ATOFMS.[12]

4   Results and discussion

4.1   Bulk mass concentrations

Concentrations of $PM_{2.5}$, PM_{10} and O_3 from both the IM and EM simulations are first compared to the observations from the BDQA database to evaluate the model performance. Table 2 shows the definitions of the statistical indicators used in this study, while Table 3 compares the results from the IM and EM simulations with the measurements over the entire simulation period. Both the EM and IM simulations have good model performance, as the hourly O_3 concentration satisfies the recommended performance criteria[44] ($|MNGB| \leq 15\%$ and MNGE $\leq$ 30%), and both PM_{10} and $PM_{2.5}$ meet the model performance criteria proposed by Boylan and Russell[45] with MFE $\leq$ 75% and $|MFB| \leq 60\%$. The statistics for $PM_{2.5}$ are even closer to the model performance goal (MFE $\leq$ 50% and $|MFB| \leq 30\%$) proposed by Boylan and Russell,[45] while PM_{10} is rather under-estimated, which is consistent with previous simulations over the same region.[27,36,46] Possible reasons for this under-estimation of coarse particles may be that re-suspension is not modelled and that boundary conditions (*i.e.*, pollution transported into Greater Paris from other regions) may be under-estimated.

The concentrations of PM_{10} and $PM_{2.5}$ from the IM and EM simulations are very similar, which is consistent with the findings of the summer simulations.[27] However, the similarity between PM_{10} and $PM_{2.5}$ from the IM and EM simulations may be artificial, as it may be caused by the bulk equilibrium approach used to compute the condensation/evaporation of organics. Organic mass is found to be the largest component of the total aerosol mass here. As shown in Zhu *et al.*[27] for

Table 2 Definitions of the statistics used in this work. $(o_i)_i$ and $(c_i)_i$ are the observed and the simulated concentrations at time and location i, respectively. n is the number of data

Statistic indicator	Definition
Root mean square error (RMSE)	$\sqrt{\dfrac{1}{n}\sum\limits_{i=1}^{n}(c_i-o_i)^2}$
Correlation	$\dfrac{\sum\limits_{i=1}^{n}(c_i-\bar{c})(o_i-\bar{o})}{\sqrt{\sum\limits_{i=1}^{n}(c_i-\bar{c})^2}\sqrt{\sum\limits_{i=1}^{n}(o_i-\bar{o})^2}}$
Mean normalised gross bias (MNGB)	$\dfrac{1}{n}\sum\limits_{i=1}^{n}\dfrac{o_i-c_i}{c_i}$
Mean normalised gross error (MNGE)	$\dfrac{1}{n}\sum\limits_{i=1}^{n}\dfrac{|o_i-c_i|}{c_i}$
Normalised mean bias (NMB)	$\dfrac{\sum\limits_{i=1}^{n}o_i-c_i}{\sum\limits_{i=1}^{n}c_i}$
Normalised mean error (NME)	$\dfrac{\sum\limits_{i=1}^{n}|o_i-c_i|}{\sum\limits_{i=1}^{n}c_i}$
Mean fractional bias (MFB)	$\dfrac{1}{n}\sum\limits_{i=1}^{n}\dfrac{c_i-o_i}{(c_i+o_i)/2}$
Mean fractional error (MFE)	$\dfrac{1}{n}\sum\limits_{i=1}^{n}\dfrac{|c_i-o_i|}{(c_i+o_i)/2}$

inorganics, the mixing assumption strongly impacts the concentrations of semi-volatile components when the condensation/evaporation is computed dynamically.

More detailed analyses are made for PM_1 by comparing individual chemical components in the model simulations with the observation data from Healy *et al.*[12] Because dust and sea-salt are not taken into account in the measurements

Table 3 Statistics for the IM and EM simulation results (15 January to 11 February) and measurements of the BDQA network during the MEGAPOLI winter campaign. (Obs. stands for observation. Sim. stands for simulation. Corr. stands for correlation)

Species	Sim.	Obs. mean µg m^{-3}	Sim. Mean µg m^{-3}	RMSE µg m^{-3}	Corr.%	MNGB%	MNGE%	MFB%	MFE%
O$_3$	IM	31.59	37.07	18.72	61.23	−2.78	20.44	−8.13	23.71
	EM	31.59	37.07	18.72	61.23	−2.78	20.44	−8.13	23.71
PM$_{10}$	IM	30.68	19.63	22.49	38.26	−24.33	51.06	−46.64	63.34
	EM	30.68	19.44	22.65	37.86	−25.10	51.41	−47.69	64.08
PM$_{2.5}$	IM	24.95	21.65	19.02	39.58	19.53	66.86	−9.39	55.57
	EM	24.95	21.53	19.21	38.65	19.55	67.73	−10.08	56.28

of Healy $et\ al.$,[12] they are not included in the computation of simulated PM_1 concentrations for the comparison. In other words, PM_1 is computed by summing the concentrations of the first three size bins (between 0.01 μm and 1 μm) and all composition bins, excluding the concentrations of dust and sea salt. The concentrations of elemental carbon (EC), sulfate (SO_4), nitrate (NO_3), ammonium (NH_4), organic aerosols (OA) in PM_1 are available in the measurements and are compared to the simulation results. The statistical performance of the IM and EM simulations is presented in Table 4 with the measurements for the entire simulation period. The temporal evolution of the different chemical components is plotted in Fig. 2.

Over the entire simulation period, Table 4 and Fig. 2 show that both the IM and EM results compare well to observations. The statistics for comparisons of PM_1 and EC meet both the model performance goal and criterion proposed by Boylan and Russell,[45] while the statistics of the other components meet the model performance criterion. EC, SO_4 and NO_3 are slightly under-estimated, while OA and NH_4 are slightly over-estimated. SO_4 tends to be more under-estimated during the first two weeks because of the under-estimation of some events, as shown in Fig. 2. On 18 January, an increase in SO_4 was caused by a strong fog event. The model is not able to reproduce this peak, as fog events may not be properly modelled in our simulations, where cloud chemistry occurs depending on the liquid water content of the grid cell. This also explains the under-estimation of the peak concentrations of NO_3 and NH_4 during the same period. The under-estimation of sulfate may also be linked to the formation of organo-sulfate, as Healy $et\ al.$[12] observed internally-mixed organics and sulfate during that fog event. Another peak of SO_4 occurs between 25 and 28 January, where highly polluted continental air masses, which most likely originated from north-western and eastern Europe, are transported over Greater Paris.[12] The under-estimation of this peak may be due to uncertainties in the larger-scale simulations (France and Europe), leading to an under-estimation of the amount of sulfate transported into

Table 4 Statistics for the IM and EM simulation results (15 January to 11 February) and measurements obtained[12] at the LHVP site (48.75°N, 2.36°E) during the MEGAPOLI winter campaign (Obs. stands for observation. Sim. stands for simulation. Corr. stands for correlation)

| Species	Sim.	Obs. mean μg m^{-3}	Sim. Mean μg m^{-3}	RMSE μg m^{-3}	Corr.%	NMB%	NME%	MFB%	MFE%
PM_1	IM	14.21	12.16	9.53	59.47	−14.42	43.45	−8.83	45.84
	EM	14.21	11.99	9.62	59.06	−15.60	43.82	−10.62	46.52
EC	IM	2.08	1.46	1.42	46.82	−29.59	46.56	−26.33	49.35
	EM	2.08	1.47	1.41	46.90	−29.45	46.54	−26.16	49.30
SO_4	IM	1.62	0.84	1.82	54.52	−48.48	65.34	−31.36	70.14
	EM	1.62	0.83	1.83	53.55	−49.04	65.91	−33.02	71.30
NO_3	IM	3.59	2.20	2.85	64.79	−38.73	49.15	−39.47	61.79
	EM	3.59	2.23	2.77	67.57	−37.90	49.06	−40.67	64.49
NH_4	IM	1.15	1.54	1.10	61.47	33.42	70.29	38.98	69.07
	EM	1.15	1.34	0.95	61.88	15.74	59.62	32.64	65.12
OA	IM	4.65	6.20	6.41	38.72	33.19	77.86	10.28	60.59
	EM	4.65	6.21	6.42	38.79	33.44	77.99	10.42	60.64
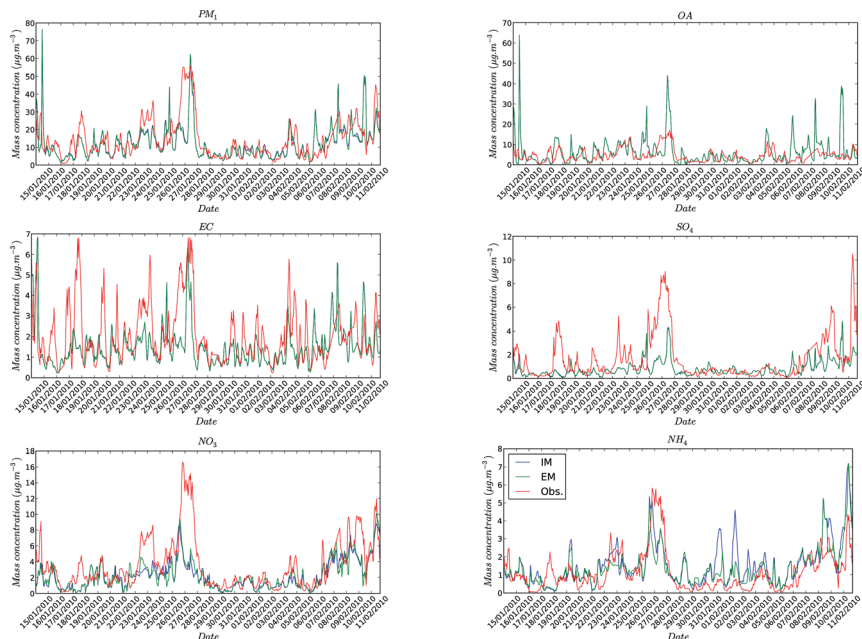
Fig. 2 Comparisons of the IM (blue line) and the EM (green line) simulation results with ATOFMS-derived mass concentrations for PM_1, EC, OA and inorganic ions (Obs. stands for observation – red line), when only the green line is visible the difference between the runs (IM $vs.$ EM) is less than the thickness of the line.

Greater Paris through boundary conditions. Such under-estimation of sulfate has been observed in previous simulations over Europe during the winter period of 2001,[28] and likely originates from uncertainties in sulfur aqueous chemistry. As emphasized by Bessagnet et $al.$,[47] sulphur aqueous chemistry, which is predominant in winter, is very difficult to simulate, because it is very sensitive to temperature and pH. Note that during the same event, EC is relatively well modelled, while OA is over-estimated. There is no peak of SO_4 during the period 28 January–7 February, which is dominated by local emissions and is well modelled.

As for PM_{10} and $PM_{2.5}$, the differences in PM_1 concentrations between the IM and EM simulations are not significant, although noticeable differences occur in the NO_3 and NH_4 peaks, as shown in the time evolution curves of Fig. 2. As expected, both the IM and EM simulations lead to similar concentrations of non-volatile components (EC, SO_4) and also of OA (because of the bulk-equilibrium assumption made when computing condensation/evaporation of organics). Because EC, SO_4 and OA represent more than 71% of the PM_1 concentration, the variations of the PM_1 concentration with the mixing-state hypothesis are limited. For volatile inorganics (NO_3 and NH_4), the EM assumption results in higher NO_3 concentration and lower NH_4, as noted in the summer simulations.[27] The modelled mass concentrations for NH_4 are lower in the EM scenario, between 30 January and 3 February (see Fig. 2), which is more consistent with observations.

Fig. 3 represents the size distribution of mass concentration and mass fraction for each chemical species. Compared to Healy et $al.$,[12] a similar distribution is found for EC with higher concentrations at low diameters (<200 nm), and for secondary
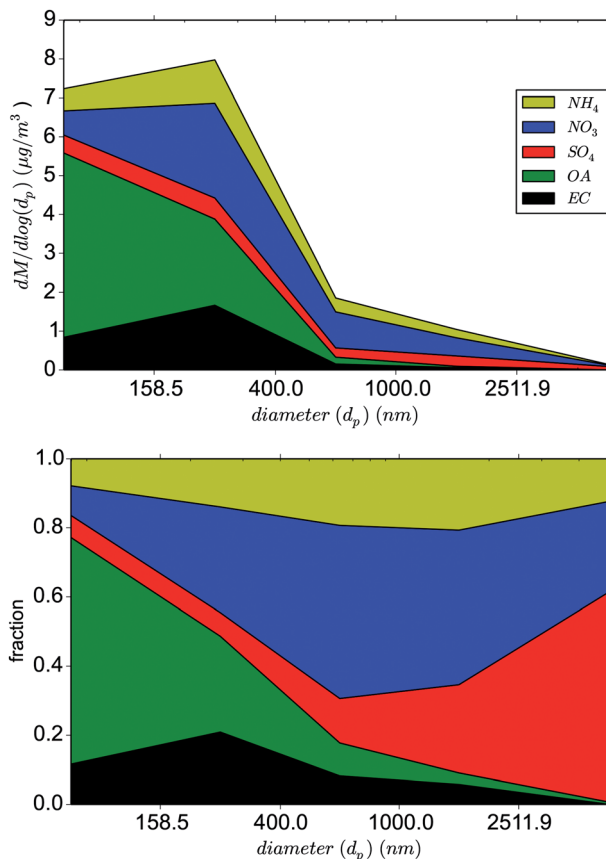
Fig. 3 Mass-size distribution (up, stacked) and size-resolved average mass fractions (down, stacked) for each chemical species from the external mixing simulation.

inorganic components such as NO_3, SO_4 and NH_4, larger mass fractions are found at higher diameters (>400 nm). However, in contrast to the measurements, most of the OA mass is found in the smallest size bins, probably because of the redistribution algorithm used in the condensation/evaporation of organics, which neglects the Kelvin effect. The condensation/evaporation of organics is performed using a bulk-equilibrium approach, which determines, for each organic chemical component, the gas-phase concentration and the particle-phase concentration summed over all size and composition bins. The condensed OA concentration is redistributed onto particle bins depending on the number concentrations of the bins and their mean diameters. In order to improve the size distribution of OA, the redistribution of the OA mass should be improved by taking the Kelvin effect into account in the redistribution algorithm (see ESI† for more detailed discussions), or by computing dynamically the condensation/evaporation of OA.

4.2 Concentrations of particle composition classes

In the EM simulation, 17 particle classes are discretised based on the combinations of the mass-fraction bins of the different chemical components (or groups of

chemical components), as defined in Table 1. The chemical group OT contains NH_4, dust and sea salt. However, as dust and sea salt are not included in the measurements of Healy *et al.*,[12] they are not considered when computing particle total mass, and the composition of each particle class is therefore recomputed after the simulation. In the updated particle classes, the only component considered in the group OT is NH_4. Table S1† shows the average mass fraction of each chemical component at the LHVP site for PM_1 particles, as well as the mass fraction of each particle class within the PM_1 concentration. It is clear that most of the particle mass is concentrated in a few particle classes. OA dominated particles represent more than half of the total particle mass (60.1%), while the rest of the particle mass is represented by the classes OA–NO_3 (19.8%), EC–OA (13.1%), EC (2.9%), OA–SO_4 (1.3%) and EC–OA–NO_3 (1.0%). The particle composition classes from the simulation and measurements are classified so that they can be easily compared. The details of the classification are presented in the ESI,† together with the mass fraction of the chemical components of each particle class (Tables S2 and S3†).

The mixing state of EC is well reproduced in the simulation (Table 5). As shown in Tables S2 and S3,† the simulation results estimate 18.0% of EC-rich particles and 82.0% of EC-poor particles, in excellent agreement with the ratio from the measurements: 16.8% EC-rich particles and 83.2% EC-poor particles. Furthermore, 10.3% of EC particles are found to be mixed with OA (EC–OA class) in the measurements against 13.1% in the simulation. The percentage of EC–OA–NO_3 particles is under-estimated in the simulation (1.1%) compared to the measurements (3.8%), as well as the percentage of EC–OA–SO_4 particles (0.2% in the simulation compared to 2.7% in the measurements). In the measurements, EC–OA–SO_4 particles have the highest concentrations during the fog event, indicating that the under-estimation of EC–OA–SO_4 particles in the simulation is probably linked to the fog event when sulfate concentrations are strongly under-estimated in the simulation.

As for the total EC, the mixing state of EC-rich particles is relatively well simulated. In the simulation (see Table S1†), more than 84% of EC-rich particles are mixed (with a mass fraction of EC lower than 90%). In the measurements, all EC-rich particles are found mixed with other species. This is slightly higher than determined in the simulation, partly because in the measurements the classification was originally based on sources rather than mass fractions of the different chemical components. The average mass fraction of EC is around 0.45 for all EC-rich particles in the simulation, which is close to the value from the

Table 5 Mass fractions of each chemical group for EC-rich and EC-poor particles from both observation (Obs.) and simulation (Sim.)

| Cases | Particle class | Mass ratio% | Mass fraction of each group | | | | |
			EC	SO_4	NO_3	OA	NH_4
Obs.	EC-rich	16.8	0.48	0.10	0.08	0.31	0.03
	EC-poor	83.2	0.07	0.14	0.32	0.36	0.11
Sim.	EC-rich	18.04	0.45	0.02	0.03	0.48	0.02
	EC-poor	81.96	0.01	0.03	0.08	0.83	0.05

measurements (0.48). This indicates that the average degree of mixing of EC-rich particles is similar between simulation and measurements. However, the mixing state of EC-poor particles is not as well simulated as the mixing state of EC-rich particles. Most of the EC-poor particles are nearly unmixed (73%) in the simulation, while all of the particles are found to be well mixed (with OA mass fraction between 0.27 and 0.52) from the measurements. Most of the mass of EC-poor particles is represented by OA, as indicated by the high value (0.83) of the OA mass fraction for the EC-poor particles from the simulation. These EC-poor particles tend to have low diameters (92% below 0.4 μm). The over-estimation of the percentage of OA in these EC-poor particles is a consequence of the redistribution algorithm used in the condensation/evaporation of organics, as discussed in the previous section.

Table 6 presents the statistics for EC-rich and EC-poor particles where a relatively good correlation can be found for both EC-rich and EC-poor particles (43.1% and 60.5% respectively). The statistics of EC-poor particles even satisfy the model performance goal of Boylan and Russell[45] for PM simulation. The statistics of EC-rich particles are not as good as those of EC-poor particles, because the particle mass is under-estimated due to the underestimation of EC, NO_3 and SO_4 (EC-rich particles not only contain EC mass, but also the mass of the other species mixed with EC). Nevertheless, these results show that the SCRAM model can simulate the concentrations of EC-rich and EC-poor particles reasonably well.

4.3 Mixing state analysis

Healy et al.[1] compute a quantitative mixing-state index (χ) of measured particles based on the information-theoretic entropy approach proposed by Riemer and West.[48] The same method is used in this study to derive the mixing-state index of simulated particles. A detailed description of this method can be found in Riemer and West.[48] For a population of N particle compositions ($N = 17$ in this study) and A distinct chemical components (or species, $A = 5$ in this study), the mass of species a in particle i is denoted as μ_i^a for $i = 1, ..., N$ and $a = 1, ..., A$; the total mass of particle i is μ_i; the total mass of species a in the total particle population is μ^a, and the total mass of the entire population is μ. These masses are computed as follows:

$$\mu_i = \sum_{a=1}^{A} \mu_i^a \quad \mu^a = \sum_{i=1}^{N} \mu_i^a \quad \mu = \sum_{i=1}^{N} \mu_i^a = \sum_{a=1}^{A} \mu^a \tag{1}$$

Table 6 Statistics for EC-rich and EC-poor particles obtained in simulations (15–28 January) and measurements obtained[12] at the LHVP site (48.75°N, 2.36°E) (Obs. stands for observation. Sim. stands for simulation. Corr. stands for correlation)

Particle class	Obs. mean μg m^{-3}	Sim. mean μg m^{-3}	RMSE μg m^{-3}	Corr.%	NMB%	NME%	MFB%	MFE%
EC rich	4.77	2.14	3.71	43.11	−55.13	63.11	−83.68	89.96
EC poor	11.82	9.85	8.46	60.50	−16.68	45.56	−7.61	48.98

The mass fraction of species a in particle i (p_i^a), the mass fraction of particle i in the population (p_i), and the mass fraction of species a in the population (p^a) can be calculated as follows:

$$p_i^a = \frac{\mu_i^a}{\mu_i} \quad p_i = \frac{\mu_i}{\mu} \quad p^a = \frac{\mu^a}{\mu} \tag{2}$$

This information can be computed either for particles within each size bin or for particles merged from several size bins. In this study, for comparison with measurements of PM_1, the analysis is performed for particles in the first three size bins (10–1000 nm).

The information-theoretic Shannon entropy is a measure of the uncertainty associated with a random variable. According to Riemer and West,[48] the Shannon entropy associated with each single particle (H_i) can be computed based on the mass fraction of each species within that particle:

$$H_i = \sum_{a=1}^{A} -p_i^a \ln p_i^a \tag{3}$$

While the average per-particle Shannon entropy (H_α) is given by:

$$H_\alpha = \sum_{i=1}^{N} -p_i H_i \tag{4}$$

Finally, the Shannon entropy of the entire bulk population (H_γ) can be expressed as:

$$H_\gamma = \sum_{a=1}^{A} -p^a \ln p^a \tag{5}$$

Based on these Shannon entropies, the corresponding diversity values can be derived:

$$D_i = e^{H_i} \quad D_\alpha = e^{H_\alpha} \quad D_\gamma = e^{H_\gamma} \tag{6}$$

where D_i is the particle diversity, or the effective number of species in particle i, D_α is the average single particle diversity, and D_γ is the bulk population diversity.

Finally, the mixing-state index χ can be derived from the following equation:

$$\chi = \frac{D_\alpha - 1}{D_\gamma - 1} \times 100\% \tag{7}$$

To summarize, D_i represents the number of chemical components in a particle, D_α represents the average value of D_i over the entire particle population, and D_γ shows the bulk population diversity which is consistent under both IM and EM assumptions. Eventually, χ represents the degree of similarity between an arbitrary mixing case and a pure internal mixture. As a result, $\chi = 0\%$ for a pure external mixture, because $D_i = D_\alpha = 1$, while $\chi = 100\%$ for a pure internal mixture as $D_\alpha = D_\gamma$.

The single particle diversity (D_i) is computed from the simulation results and compared to the measurements at the LHVP site. Most of the simulated particles (64.5%) are within the D_i range 1.8 to 3.0, which is very close to the value of 71% obtained by Healy et al.[1] for the same D_i range. As most particles are concentrated in the smallest size bins, the D_i values are normalised by the number of particles in each size bin in order to get a better representation of the variation of D_i with particle size. Fig. 4 shows the dependence of the time-averaged number concentration on diversity and particle diameter, as well as the dependence of time-averaged particle composition on particle diameter. As noted by Healy et al.,[1] smaller particles have higher mass fractions of EC and OA, while larger particles have higher inorganic mass fractions. Although the particle number concentrations tend to be under-estimated in the simulation, high number concentrations are observed at low diameters (below 200 nm) for low diversities (between 1.8 and 2.3 in the measurements and between 1.8 and 3 in the simulation) and at high diameters for high diversity (between 3.6 and 4.2 in the measurements and between 3.4 and 4.2 in the simulation). In agreement with the measurements, at low diameters, most of the particles are composed of 2 or 3 species, mainly OA and EC. At high diameters, particles are composed of inorganics (80% in the simulation and 60% in the measurements). As the particle diameter grows, the mass fraction of inorganics also grows in the measurements, indicating that the condensation/evaporation of inorganic species is correctly modelled. However, the OA mass is under-estimated at high diameters and over-estimated at low diameters, indicating as noted before that the redistribution of OA after condensation/evaporation needs to be improved or to be computed dynamically.

As in the measurements, the mass fraction of EC decreases from 26% for the bin of diameters between 158.6 nm and 400 nm to a value lower than 10% at higher diameters. The variation of EC with particle diameter is largely linked to
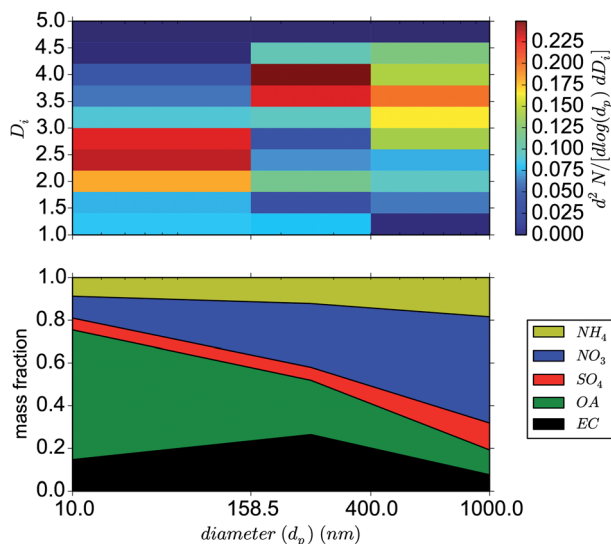

Fig. 4 Dependence of the time-averaged number concentration on single particle diversity (diversity normalised by the number of particles in each bin) and particle diameter (upper panel), and dependence of time-averaged particle composition on particle diameter (lower panel).

the size distribution used in the emissions: 54% was emitted in the bin [10–158.5 nm], 42% in the bin [158.5–400 nm] and 3% in the bin [400–1000 nm]. Although the mass fraction of EC increases to about 52% in the measurements, it remains below 30% in the simulation, because of the over-estimation of OA at low diameters, as well as the assumed size-distribution of emissions.

The average single particle diversity (D_α) and the species diversity of the bulk population (D_γ) are also derived from the simulation results. Unlike D_i, which represents the characteristics of a single particle, D_α and D_γ describe the overall attributes of the entire particle population. The mixing-state index χ can potentially range from 0% (fully externally mixed) to 100% (fully internally mixed). The averaged value of D_α from the simulation (2.91) is close to that obtained from the measurements (2.79), while that averaged value of D_γ tends to be under-estimated (3.76 from the simulation and 4.04 from the measurements), because of the bulk over-estimation of OA and the bulk under-estimation of SO_4. As a result, the mixing-state index χ is slightly over-estimated (69% in the simulation and 59% in the measurements), although the average single particle diversity is well represented. These values of the mixing-state index indicate that the particle population at LHVP is not internally mixed.

The relationship between D_α, D_γ and χ at the LHVP site is displayed in Fig. 5. The values of the mixing-state index range from 23% to 90%, with a mean value of 69%. This result is generally consistent with the measurements of Healy et al.,[1] where the mixing-state index is found to vary between 37% and 72%, with a mean value of 59%. Another phenomenon observed from the measurements, and also apparent in Fig. 5 is that the average single particle diversity (D_α) is never higher than 4 (3.5 in the measurements), even when the bulk population diversity (D_α) approaches the maximum value of 5. This indicates that a variety of different chemical mixing states exist for particles of the same size at all times.
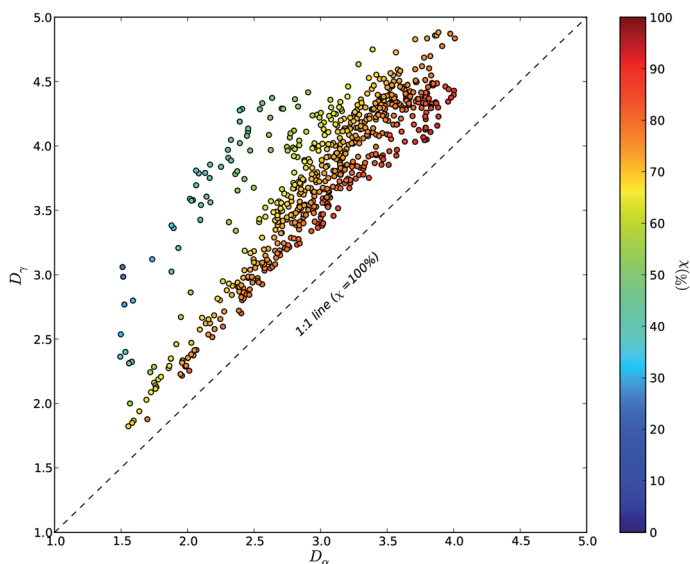

Fig. 5 Scatter plot of the hourly mixing-state index (χ) as a function of average particle diversity (D_α) and average bulk population diversity (D_γ).

The diurnal variations of D_α, D_γ and χ are computed from both simulation and observation results, and the dependence of their mean value upon time of day is shown in Fig. 6, as well as the corresponding variation of the mass fraction of each chemical component. The averaged value of D_α from the simulation (2.91) is very close to the one from the measurement (2.79). However, D_γ is relatively underestimated from the simulation due to the overestimation of OA and underestimation of SO_4. As a result, the mixing-state index χ is overestimated. A decrease of both D_α and χ can be observed between 5:00 and 8:00 in the simulation, due to the increase of traffic emissions, which introduce a large amount of particles with high EC mass fractions and low D_i values. However, D_γ does not increase during this period, as suggested by the measurements because of the increase of the mass fraction of EC and OA. In both the simulation and the measurements, the value of χ increased between 8:00–14:00 due to the combined effect of increasing D_α and decreasing D_γ. The increase of D_α during this period is due to the decrease of traffic emissions and ageing of existing particles, while the decrease of D_γ is largely caused by the increase of the OA fraction and the decrease of the EC and inorganic fractions. In the simulation, χ drops between 14:00 and 20:00 due to the increase of D_γ as a result of slowly increasing EC mass fraction (evening traffic). However, this decrease is limited to 14:00–16:00 in the measurements. An increase of D_α can be observed between 20:00 and 22:00 in both the simulation and the measurements, as a result of enhanced ammonium nitrate during night
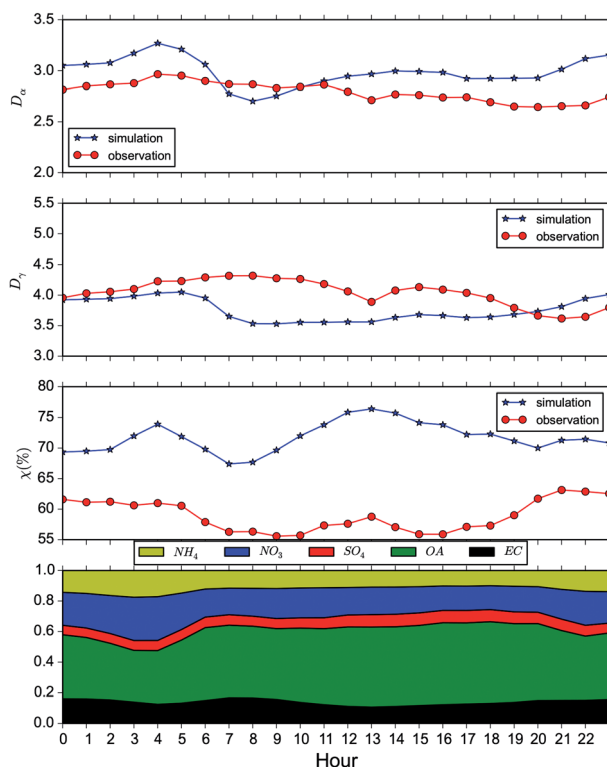

Fig. 6 Diurnal variations of the mixing-state index (χ) and bulk population mass fraction.

time, which is reflected by the increase of inorganic mass fraction during that period, as well as an increase of D_γ.

So far, the discussion was based on the measurements and simulation results at the LHVP site. Because our modelling study provides comprehensive data for the study of the spatial distribution of particle properties, Fig. 7 presents the spatial distribution of D_α, D_γ and χ over the entire simulated domain, averaged over the simulation period. The values of D_α are lower close to the centre of Paris and in areas with significant traffic but higher in rural areas. Diversity is lower where emissions are high, because freshly emitted particles mostly consist of one chemical component with a single particle diversity close to 1. The spatial distribution of D_γ is relatively uniform as it represents the number of bulk chemical components. However, there are regions where D_γ can suddenly increase or decrease, and these variations may not be similar to those of D_α. For example, in the region within the black rectangle in Fig. 7 (strong dust emissions from sand and stone mining industries along the Seine river), some parts have low D_γ and low D_α. This type of region (low D_α and low D_γ) may imply a relatively homogeneous emission source, where only one type of particle is emitted. Other regions, such as the south west of Paris and Roissy airport (denoted by the black circle in Fig. 7) have low D_α values and high D_γ values. In such regions, there may be heterogeneous emission sources, where particles with distinct compositions may be emitted from the same place or transported to that place. Considering the spatial distribution of the mixing-state index χ, regions with a larger difference between D_α and D_γ usually have lower χ, which means they are less internally mixed. Usually, the regions of low χ correspond to regions of low D_α (high traffic emissions). Note that for regions of low D_α but low D_γ, such as within the black rectangle in Fig. 7, the mixing-state index can be high, although the region may
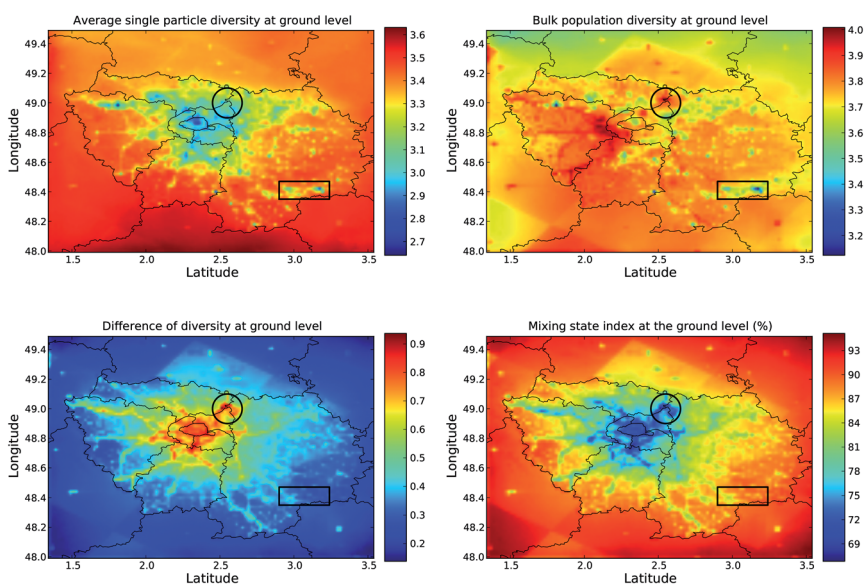

Fig. 7 Spatial distribution of time-averaged average single particle diversity (D_α), average bulk population diversity (D_γ), difference between D_α and D_γ, and mixing-state index (χ) over Greater Paris.

correspond to a location characterised by strong local emissions. Thus, χ also reflects the homogeneity of the particle population, and a group of particles with a heterogeneous composition has a low mixing-state index and is considered as externally mixed. On the other hand, a group of particles with a homogeneous composition has a high mixing-state index and is considered as internally mixed, even if the dominant particles consist of only one species (from one source).

5   Conclusions

Particle diversity and mixing state was studied using the newly developed size-composition resolved aerosol model (SCRAM) coupled to the Polyphemus air-quality platform. Two simulations were conducted over Greater Paris with different mixing-state assumptions (internal mixing IM or external mixing EM).

Both simulations reproduce well the concentration of O_3, PM_{10} and $PM_{2.5}$, as assessed from comparisons to observations from the BDQA network. The simulation results of both bulk concentrations of chemical species and the concentrations of individual particle classes are compared with the observations of Healy et al.[12] Good correlations are found between simulation results and measurements for both PM_1 and bulk species concentrations, and the statistical indicators for most species satisfy the model performance criteria proposed by Boylan and Russell,[45] although the concentration of SO_4 is under-estimated during periods where significant chemical processing occurs, e.g. during a strong fog event and periods dominated by continental (aged) air masses.

For the concentrations of individual particles obtained from the EM simulation, a very good agreement is found for the mass fractions of EC-rich and EC-poor particles between simulation results and observations. The single particle diversity and mixing-state index are computed from the results of the EM simulation based on a new quantification approach developed by Riemer and West,[48] and are compared with the observation based analyses of Healy et al.[1] at the urban site LHVP. The average value of the single particle diversity is consistent between the simulation and the measurements (2.91 and 2.79, respectively), while the averaged bulk population diversity is slightly under-estimated (3.76 from the simulation and 4.04 from the observation), probably because of the under-estimation of sulfate or nitrate in the model. The mixing-state index, which depends on both the single particle diversity and the bulk population diversity, is well represented by the simulation, while a mean value of 69% from the simulation and 59% from the measurements indicates that the particles are not internally mixed. Finally, the time-averaged spatial distribution of the mixing-state index shows that particles are more externally mixed in urban regions in and around Paris, while they are more internally mixed in rural regions. This indicates that traditional aerosol models, which assume that particles are internally mixed, may be suitable for simulating rural regions, while in urbanised areas, the internal-mixing assumption does not hold.

References

1 R. M. Healy, N. Riemer, J. Wenger, M. Murphy, M. West, L. Poulain, A. Wiedensohler, I. O'Connor, E. McGillicuddy, J. Sodeau, et al., Atmos. Chem. Phys., 2014, **14**, 6289–6299.

2 P. F. DeCarlo, J. R. Kimmel, A. Trimborn, M. J. Northway, J. T. Jayne, A. C. Aiken, M. Gonin, K. Fuhrer, T. Horvath, K. S. Docherty, *et al.*, *Anal. Chem.*, 2006, **78**, 8281–8289.

3 A. Petzold and M. Schönlinner, *J. Aerosol Sci.*, 2004, **35**, 421–441.

4 D. Murphy, D. Cziczo, K. Froyd, P. Hudson, B. Matthew, A. Middlebrook, R. E. Peltier, A. Sullivan, D. Thomson and R. Weber, *J. Geophys. Res.: Atmos.*, 2006, **111**, DOI: 10.1029/2006JD007340.

5 A. P. Ault, C. J. Gaston, Y. Wang, G. Dominguez, M. H. Thiemens and K. A. Prather, *Environ. Sci. Technol.*, 2010, **44**, 1954–1961.

6 R. M. Healy, J. Sciare, L. Poulain, K. Kamili, M. Merkel, T. Müller, A. Wiedensohler, S. Eckhardt, A. Stohl, R. Sarda-Estève, *et al.*, *Atmos. Chem. Phys.*, 2012, **12**, 1681–1700.

7 M. Dall'Osto, J. Ovadnevaite, D. Ceburnis, D. Martin, R. M. Healy, I. O'Connor, I. Kourtchev, J. Sodeau, J. Wenger and C. O'Dowd, *Atmos. Chem. Phys.*, 2013, **13**, 4997–5015.

8 M. Mallet, J. Roger, S. Despiau, J. Putaud and O. Dubovik, *J. Geophys. Res.: Atmos.*, 2004, **109**, DOI: 10.1029/2008JD011574.

9 H. Furutani, M. Dall'osto, G. C. Roberts and K. A. Prather, *Atmos. Environ.*, 2008, **42**, 3130–3142.

10 H. Herich, L. Kammermann, B. Friedman, D. S. Gross, E. Weingartner, U. Lohmann, P. Spichtinger, M. Gysel, U. Baltensperger and D. J. Cziczo, *J. Geophys. Res.: Atmos.*, 2009, **114**, DOI: 10.1029/2003JD003940.

11 E. Crosbie, J.-S. Youn, B. Balch, A. Wonaschütz, T. Shingler, Z. Wang, W. Conant, E. Betterton and A. Sorooshian, *Atmos. Chem. Phys.*, 2015, **15**, 6943–6958.

12 R. M. Healy, J. Sciare, L. Poulain, M. Crippa, A. Wiedensohler, A. S. Prévôt, U. Baltensperger, R. Sarda-Estève, M. L. McGuire, C.-H. Jeong, *et al.*, *Atmos. Chem. Phys.*, 2013, **13**, 9479–9496.

13 E. Debry, K. Fahey, K. Sartelet, B. Sportisse and M. Tombette, *Atmos. Chem. Phys.*, 2007, **7**, 1537–1547.

14 K. Sartelet, H. Hayami, B. Albriet and B. Sportisse, *Aerosol Sci. Technol.*, 2006, **40**, 118–127.

15 M. Z. Jacobson, R. P. Turco, E. J. Jensen and O. B. Toon, *Atmos. Environ.*, 1994, **28**, 1327–1338.

16 L. M. Russell and J. H. Seinfeld, *Aerosol Sci. Technol.*, 1998, **28**, 403–416.

17 M. Jacobson, *J. Geophys. Res.*, 2002, **107**, 1327–1338.

18 J. Lu and F. M. Bowman, *Atmos. Chem. Phys.*, 2010, **10**, 4033–4046.

19 H. Dergaoui, K. N. Sartelet, É. Debry and C. Seigneur, *J. Aerosol Sci.*, 2013, **58**, 17–32.

20 S. Zhu, K. Sartelet and C. Seigneur, *Geosci. Model Dev.*, 2015, **8**, 1595–1612.

21 M. J. Kleeman and G. R. Cass, *Environ. Sci. Technol.*, 2001, **35**, 4834–4848.

22 P. Stier, J. Feichter, S. Kinne, S. Kloster, E. Vignati, J. Wilson, L. Ganzeveld, I. Tegen, M. Werner, Y. Balkanski, *et al.*, *Atmos. Chem. Phys.*, 2005, **5**, 1125–1156.

23 S. Bauer, D. Wright, D. Koch, E. Lewis, R. McGraw, L.-S. Chang, S. Schwartz and R. Ruedy, *Atmos. Chem. Phys.*, 2008, **8**, 6003–6035.

24 N. Oshima, M. Koike, Y. Zhang, Y. Kondo, N. Moteki, N. Takegawa and Y. Miyazaki, *J. Geophys. Res.*, 2009, **114**, 1–17.

25 N. Riemer, M. West, R. A. Zaveri and R. C. Easter, *J. Geophys. Res.*, 2009, **114**, D09202.

26 V. Mallet, D. Quélo, B. Sportisse, M. Ahmed de Biasi, É. Debry, I. Korsakissok, L. Wu, Y. Roustan, K. Sartelet, M. Tombette, *et al.*, *Atmos. Chem. Phys.*, 2007, 7, 5479–5487.

27 S. Zhu, N. K. Sartelet, Y. Zhang and A. Nenes, *J. Geophys. Res.*, 2016, accepted.

28 K. Sartelet, E. Debry, K. Fahey, Y. Roustan, M. Tombette and B. Sportisse, *Atmos. Environ.*, 2007, **41**, 6116–6131.

29 G. Sarwar, D. Luecken, G. Yarwood, G. Z. Whitten and W. P. Carter, *Journal of Applied Meteorology and Climatology*, 2008, **47**, 3–14.

30 K. M. Fahey and S. N. Pandis, *Atmos. Environ.*, 2001, **35**, 4471–4478.

31 A. Nenes, S. N. Pandis and C. Pilinis, *Aquat. Geochem.*, 1998, **4**, 123–152.

32 F. Couvidat, É. Debry, K. Sartelet and C. Seigneur, *J. Geophys. Res.: Atmos.*, 2012, **117**, DOI: 10.1029/2011JD017214.

33 L. W. Horowitz, S. Walters, D. L. Mauzerall, L. K. Emmons, P. J. Rasch, C. Granier, X. Tie, J.-F. Lamarque, M. G. Schultz, G. S. Tyndall, *et al.*, *J. Geophys. Res.: Atmos.*, 2003, **108**, DOI: 10.1029/2002JD002853.

34 V. Vestreng, *Review and Revision. Emission data reported to CLRTAP. EMEP MSC-W Status Report 2003*, Meteorological synthesizing centre–west, norwegian meteorological institute, oslo technical report, 2003.

35 A. Guenther, T. Karl, P. Harley, C. Wiedinmyer, P. Palmer and C. Geron, *Atmos. Chem. Phys.*, 2006, **6**, 3181–3210.

36 F. Couvidat, Y. Kim, K. Sartelet, C. Seigneur, N. Marchand and J. Sciare, *Atmos. Chem. Phys.*, 2013, **13**, 983–996.

37 A. Charron and G. Aymoz, *PM-DRIVE: Particulate DiRect and Indirect On-Road Vehicular Emissions*, L'agence de l'environnement et de la maîtrise de l'energie (ademe) technical report, 2015.

38 W. Skamarock, J. Klemp, J. Dudhia, D. Gill, D. Barker, M. Duda, X. Huang, W. Wang and J. Powers, *A description of the advanced research WRF version 3*, NCAR Technical Note, NCAR/TN\ u2013475? STR, 2008, p. 123.

39 Y. Kim, K. Sartelet, J.-C. Raut and P. Chazette, *Boundary-Layer Meteorology*, 2013, **149**, 105–132.

40 S.-Y. Hong, Y. Noh and J. Dudhia, *Mon. Weather Rev.*, 2006, **134**, 2318–2341.

41 S.-Y. Hong and J.-O. J. Lim, *Asia-Pacific Journal of Atmospheric Sciences*, 2006, **42**, 129–151.

42 J. S. Kain, *J. Appl. Meteorol.*, 2004, **43**, 170–181.

43 D. S. Gross, R. Atlas, J. Rzeszotarski, E. Turetsky, J. Christensen, S. Benzaid, J. Olson, T. Smith, L. Steinberg, J. Sulman, *et al.*, *Environ. Model. Software*, 2010, **25**, 760–769.

44 A. Russell and R. Dennis, *Atmos. Environ.*, 2000, **34**, 2283–2324.

45 J. W. Boylan and A. G. Russell, *Atmos. Environ.*, 2006, **40**, 4946–4959.

46 Y. Wang, K. N. Sartelet, M. Bocquet and P. Chazette, *Atmos. Chem. Phys.*, 2014, **14**, 3511–3532.

47 B. Bessagnet, A. Hodzic, R. Vautard, M. Beekmann, S. Cheinet, C. Honoré, C. Liousse and L. Rouil, *Atmos. Environ.*, 2004, **38**, 2803–2817.

48 N. Riemer and M. West, *Atmos. Chem. Phys.*, 2013, **13**, 11423–11439.